

Efficient Direct H₂O₂ Synthesis Enabled by PdPb Nanorings via Inhibiting the O–O Bond Cleavage in O₂ and H₂O₂

Kailei Cao,[#] Hao Yang,[#] Shuxing Bai, Yong Xu,* Chengyong Yang, Yu Wu, Miao Xie, Tao Cheng, Qi Shao, and Xiaoqing Huang*



Cite This: ACS Catal. 2021, 11, 1106–1118



Read Online

ACCESS |

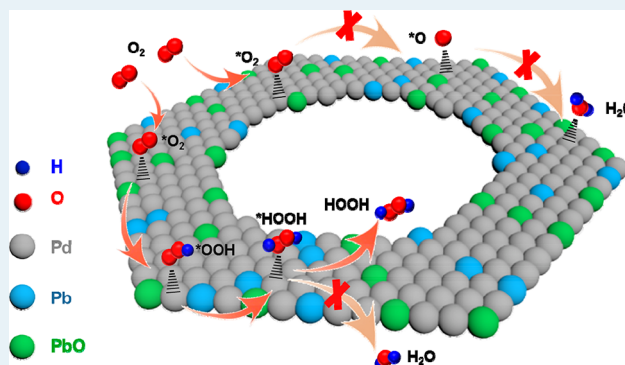
Metrics & More

Article Recommendations

Supporting Information

ABSTRACT: Direct H₂O₂ synthesis (DHS) from H₂ and O₂ is a promising process in industry; however, challenges related to poor H₂O₂ selectivity and low H₂O₂ yield remain. We report here that Pd_xPb nanorings (NRs) can serve as high-efficiency catalysts for DHS. We demonstrate that the preferential location of Pb species at the edge and corner can significantly decrease the amount of low-coordinated Pd atoms in Pd_xPb NRs, leading to an enhanced H₂O₂ yield and selectivity but a reduced degradation rate. Consequently, the optimized catalyst gives a H₂O₂ yield of 170.1 mol kg_{cat}⁻¹ h⁻¹, being one of the best catalysts reported for DHS to the best of our knowledge. Theoretical calculations reveal that Pd_xPb NRs are favorable for *OOH formation, a key intermediate for DHS, while Pd NRs tend to dissociate O₂ to form H₂O in the presence of H₂. On the other hand, the cleavage of O–O in H₂O₂ is strongly suppressed on Pd_xPb NRs, leading to a low H₂O₂ degradation rate. This work highlights the significance of catalyst surface modifications, especially the control of Pd coordination environment on DHS performance, which may provide deep insight for catalyst design in heterogeneous catalysis.

KEYWORDS: low-coordinated, palladium, surface modification, direct H₂O₂ synthesis, catalysis



1. INTRODUCTION

Hydrogen peroxide (H₂O₂) is among the most important chemicals in industry for the production of fine chemicals and medicine, rocket fuels, sterilization, bleaching, and so on.^{1–5} In the conventional process, H₂O₂ is mainly produced via the anthraquinone method, which consists of hydrogenation and oxidation of anthraquinone successively.⁶ The quest for an eco-friendly process for H₂O₂ synthesis is driven by the current disadvantages including high energy consumption and heavy pollution.⁶ Under such circumstances, direct H₂O₂ synthesis (DHS) from H₂ and O₂ is considered as a clean and efficient strategy to replace the conventional process.^{7,8} Despite that tremendous effort has been devoted to developing efficient catalysts for DHS from H₂ and O₂, this process suffers from poor H₂O₂ selectivity because of the formation of H₂O, as a result of a low H₂O₂ yield. As the state-of-the-art catalyst, Pd has been widely used for DHS from H₂ and O₂, and great progress is achieved.^{9,10} However, Pd suffers from low H₂O₂ selectivity because it tends to catalyze O₂ dissociation to form H₂O in the presence of H₂, leading to a poor H₂O₂ yield.^{9–11} Moreover, H₂O₂ degradation including decomposition (2H₂O₂ → 2H₂O + O₂) and hydrogenation (H₂O₂ + H₂ → 2H₂O) on Pd will further reduce the yield of H₂O₂.^{9,10} Hence, it is highly desired to develop efficient catalysts with superior ability on

the suppression of O₂ dissociation and H₂O₂ degradation (i.e., O–O bond cleavage in O₂ and H₂O₂).

To date, several strategies have been adopted to improve the DHS performance, including the addition of inorganic acid^{12,13} or halide ions¹⁴ into the aqueous medium and catalyst modifications.^{15–17} However, the current DHS processes are facing great challenges to satisfy requirements from the chemical industry. For example, the presence of inorganic acid or halide ions requires the use of a corrosion-resistant reactor and an additional process to eliminate corrosive halide compounds in the vent gas, which may largely increase the cost for DHS.⁸ On the other hand, many composite catalysts, such as Pd–Au,^{16,17} Pd–Ni,¹⁸ Pd–Sn,¹⁰ Pd–Zn,¹⁹ and so on, have been developed for DHS with enhanced activity or selectivity. However, the lack of a complete understanding in the inherent mechanism of DHS over Pd-based catalysts has severely impeded their practical application.⁹ Therefore, more investi-

Received: October 7, 2020

Revised: December 9, 2020

Published: January 8, 2021



tigations are required to deeply reveal the structure–activity relationship and further guide chemists to develop active, selective, and stable catalysts for DHS.

Considering that H_2O formation ($\Delta G = -241.6 \text{ kJ mol}^{-1}$) is thermodynamically more favorable than H_2O_2 formation ($\Delta G = -135.8 \text{ kJ mol}^{-1}$), Pd-based catalysts generally suffer from low H_2O_2 yield because of the occurrence of side reactions (e.g., $2\text{H}_2 + \text{O}_2 \rightarrow 2\text{H}_2\text{O}$, $2\text{H}_2\text{O}_2 \rightarrow 2\text{H}_2\text{O} + \text{O}_2$ and $\text{H}_2\text{O}_2 + \text{H}_2 \rightarrow 2\text{H}_2\text{O}$).^{20–22} In principle, the selective suppression of O–O bond cleavage in O_2 (reactant) and H_2O_2 (product) is extremely critical to enhance DHS performance.^{23,24} Therefore, the ideal catalysts for DHS should be capable of improving H_2O_2 synthesis and suppressing H_2O_2 degradation simultaneously. However, the precise control of O–O bond activation on the surface of catalysts, which is vital to improve DHS performance, was overlooked in previous studies. Herein, we demonstrate that Pd_xPb nanorings (NRs) can serve as efficient catalysts for DHS. The optimized catalyst of Pd_6Pb NRs/ $\text{TiO}_2\text{-H-A}$ gives a H_2O_2 yield of $170.1 \text{ mol kg}_{\text{cat}}^{-1} \text{ h}^{-1}$, being one of the best catalysts for DHS reported to the best of our knowledge. Mechanism studies show that the preferential location of Pb species at the edge and corner significantly decreases the amount of low-coordinated Pd atoms in Pd_xPb NRs, leading to an enhanced yield and selectivity but a reduced degradation rate of H_2O_2 . Density functional theory (DFT) calculations reveal that the Pd NRs can rapidly dissociate O_2 to form H_2O in the presence of H_2 via $^*\text{O}$ intermediate species, while Pd_xPb NRs tend to activate O_2 to form $^*\text{OOH}$, a critical intermediate for H_2O_2 production. On the other hand, compared with the rapid H_2O_2 degradation rate on Pd NRs, both H_2O_2 decomposition ($2\text{H}_2\text{O}_2 \rightarrow 2\text{H}_2\text{O} + \text{O}_2$) and hydrogenation ($\text{H}_2\text{O}_2 + \text{H}_2 \rightarrow 2\text{H}_2\text{O}$) are strongly suppressed on Pd_xPb NRs, leading to a further enhancement on H_2O_2 yield. This work may not only provide an efficient catalyst for DHS but also promote the fundamental research in understanding the effects of surface modification on catalysis.

2. EXPERIMENTAL SECTION

2.1. Chemicals. Sodium tetrachloropalladate (II) (Na_2PdCl_4) was purchased from Sigma-Aldrich. Lead oxalate (PbC_2O_4), molybdenum carbonyl ($\text{Mo}(\text{CO})_6$), *N,N,N*-trimethyl-1-dodecanaminium bromide ($\text{C}_{15}\text{H}_{34}\text{NBr}$, DTAB), and polyvinylpyrrolidone (($\text{C}_6\text{H}_9\text{NO}$)_n, PVP, average M.W. 58000) were purchased from J&K Scientific Ltd. *N,N*-Dimethylformamide ($\text{HCON}(\text{CH}_3)_2$, DMF, reagent grade), methanol (CH_3OH , reagent grade), and perchloric acid (HClO_4 , Analytical Reagent, 70–72%) were purchased from Sinopharm Chemical Reagent Co. Ltd. All the chemicals were used without further purification. The water ($18 \text{ M}\Omega/\text{cm}$) used in all experiments was prepared by passing through an ultrapure purification system (Aqua Solutions).

2.2. Catalyst Preparation. *Synthesis of Pd_xPb Nanorings (NRs).* In a typical synthesis of Pd nanorings (Pd NRs), 4.8 mg of Na_2PdCl_4 , 6 mg of $\text{Mo}(\text{CO})_6$, 39 mg of DTAB, 200 mg of PVP (molecular weight: 58 000), and 5 mL of DMF were added into a 30 mL glass vial and ultrasonicated for 30 min subsequently to obtain a homogeneous mixture solution. After that, the homogeneous solution was heated from 25 to 160 °C in 0.5 h and kept for another 5 h in an oil bath. After they were cooled to room temperature, the resulting colloidal products were collected by centrifugation and washed with a mixture of ethanol/acetone for five times. The synthetic conditions for Pd_{10}Pb NRs, Pd_6Pb NRs, and Pd_4Pb NRs are similar to that of

Pd NRs synthesis except for adding 0.6, 1.2, and 2.4 mg of PbC_2O_4 , respectively.

Synthesis of TiO_2 Nanosheets (NSs). In a typical synthesis of TiO_2 nanosheets (TiO_2 NSs),²⁵ 12.5 mL of tetrabutyltitannate and 2 mL of hydrofluoric acid solution were mixed in a 30 mL glass vial under a 30 min stirring. Afterward, the mixed solution was transferred into a 20 mL Teflon-lined autoclave and subsequently treated at 180 °C for 24 h. After they were cooled to room temperature, the resulting white products were collected by centrifugation and washed with ethanol for three times, followed by drying in an oven at 70 °C for 12 h.

Preparations of Supported Catalysts. Twenty-five milligrams of TiO_2 NSs, 3 mL of ethanol, and 15 mL of chloroform were added into a 30 mL vial. After that, Pd NRs- or Pd_xPb NRs-ethanol solution was dropwise added into the above mixture under a fast stirring (1000 rpm) for 2 h. Afterward, the products were washed with acetone via centrifugation for two times and then dried in a vacuum oven at 60 °C for 12 h.

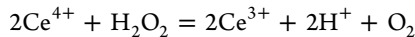
2.3. Pretreatment of Supported Catalysts. Prior to catalytic tests, the catalysts were treated at 200 °C in different atmospheres. Specifically, the catalysts calcined in H_2/Ar ($\text{H}_2/\text{Ar} = 5\%/\text{95}\%$) at 200 °C for 1 h were termed as Pd NRs/ $\text{TiO}_2\text{-H}$ and Pd_xPb NRs/ $\text{TiO}_2\text{-H}$. The catalysts calcined in dry air ($\text{O}_2/\text{N}_2 = 20\%/\text{80}\%$) at 200 °C for 1 h were named as Pd NRs/ $\text{TiO}_2\text{-A}$ and Pd_xPb NRs/ $\text{TiO}_2\text{-A}$. The catalysts were annealed in H_2/Ar ($\text{H}_2/\text{Ar} = 5\%/\text{95}\%$) at 200 °C for 1 h and then treated in dry air ($\text{O}_2/\text{N}_2 = 20\%/\text{80}\%$) for an additional 1 h under the same temperature; they were named as Pd NRs/ $\text{TiO}_2\text{-H-A}$ and Pd_xPb NRs/ $\text{TiO}_2\text{-H-A}$, respectively.

2.4. Characterizations. The morphology of the Pd and Pd_xPb NRs was characterized by a transmission electron microscope (TEM, Hitachi-HT7700, 120 kV). High-resolution TEM images (HRTEM), high angle annular dark field scanning transmission electron microscopy (HAADF-STEM) images, and elemental mapping with line-scanning were obtained on a FEI Tecnai F20 transmission electron microscope (200 kV). Atomic resolution TEM (AC-TEM) with atomic resolution was conducted on a FEI spherical aberration transmission electron microscope at an acceleration voltage of 300 kV (Titan Cubed Themis G2 300). X-ray diffraction (XRD) patterns were collected using an X'Pert-Pro X-ray powder diffractometer equipped with a Cu $\text{K}\alpha$ X-ray source ($\lambda = 0.15406 \text{ nm}$). Scanning electron microscope-energy dispersive X-ray spectroscopy (SEM-EDS) was performed on a scanning electron microscope (Hitachi, S-4700). X-ray photoelectron spectroscopy (XPS) spectra were collected by XPS (Thermo Scientific, ESCALAB 250 XI). The compositions of Pd NRs/ $\text{TiO}_2\text{-H-A}$ and Pd_xPb NRs/ $\text{TiO}_2\text{-H-A}$ were determined by inductively coupled plasma-atomic emission spectrometry (ICP-AES measurement, 710-ES, Varian). 3D tomographic reconstructions were performed on a FEI Tecnai F20 transmission electron microscope (200 kV). 2D TEM images were acquired at consecutive tilt angles from -60° to 60° with an interval of 4° . The reconstructed structure was made with the software of Avizo Version. X-ray adsorption spectroscopy (XAS) data were collected at the TPS-44A beamline of the National Synchrotron Radiation Research Center (NSRRC, Hsinchu, Taiwan) using a Si (111) quick-scanning monochromator. Data were processed according to standard procedures using the Demeter program package (Version 0.9.24). Extended X-ray adsorption fine structure (EXAFS) fitting was conducted using the software of Artemis. For H_2 -TPD measurements, 80 mg of catalyst was placed at

the bottom of the U-shaped quartz tube and pretreated in Ar flow (50 mL min^{-1}) at 300°C for 0.5 h and then cooled to 18°C . After that, the feeding H_2/Ar ($\text{H}_2/\text{Ar} = 5\%/\text{95}\%$) flowed through the catalyst bed at 18°C for 1 h. Then, Ar flow (50 mL min^{-1}) was used to remove the physisorption of H_2 at 50°C for 45 min. Finally, the catalyst bed was heated from 50 to 500°C with a heating rate of $10^\circ\text{C min}^{-1}$. A wide range of desorbing species was monitored by a thermal conductivity detector (TCD, Micromeritics AutoChem II 2920) to identify the main products generated from reactions of H_2 on the catalyst. O_2 -TPD measurement is similar to H_2 -TPD measurement except for replacing the H_2/He ($\text{H}_2/\text{He} = 5\%/\text{95}\%$) with O_2/He ($\text{O}_2/\text{He} = 5\%/\text{95}\%$). Diffuse reflectance infrared fourier transform spectroscopy (DRIFTS) measurement was conducted by a Nicolet 6700 Fourier transform infrared (FTIR) equipped with liquid nitrogen cooled mercury–cadmium–telluride detector (MCT). The wavenumber resolution is 4 cm^{-1} . The reaction chamber is DRIFTS cell (Harrick, HVC-DRP) fitted with ZnSe windows. 100 mg of sample was loaded into the cell, and subsequently, it was flushed with Ar for 0.5 h at 25°C to obtain the background spectrum. Afterward, CO/Ar ($\text{CO}/\text{Ar} = 5\%/\text{95}\%$) (40 mL min^{-1}) was flowed into the cell at room temperature for 1 h and then flushed by Ar (40 mL min^{-1}) for 0.5 h at the same temperature.

2.5. Catalyst Evaluation. Direct H_2O_2 Synthesis. Direct H_2O_2 synthesis was evaluated using a stainless-steel autoclave with a volume of 60 mL and a maximum working pressure of 10 MPa. In particular, 5 mg of supported catalyst and 8.5 mL of solvent (6.8 mL of CH_3OH and 1.7 mL of H_2O) were added into the autoclave. After being purged 3 times by Ar, 0.4 MPa of O_2 and 3.6 MPa of H_2/Ar ($\text{H}_2/\text{Ar} = 5\%/\text{95}\%$) were pressurized into the stainless-steel autoclave. The stirring rate and reaction temperature were kept at 1000 rpm and 0°C , respectively.

Evaluation of Catalytic Performance. H_2O_2 yield was determined by titrating aliquots of the final reaction solution with acidified $\text{Ce}(\text{SO}_4)_2$ (0.05 M) in the presence of two drops of ferroin indicator.¹⁰ The $\text{Ce}(\text{SO}_4)_2$ solutions were standaridized against $(\text{NH}_4)_2\text{Fe}(\text{SO}_4)_2 \cdot 6\text{H}_2\text{O}$ using ferroin as indicator. The reaction equation of generated H_2O_2 and $\text{Ce}(\text{SO}_4)_2$ is below:



Gases were analyzed by a gas chromatography (GC, Agilent 7890B) equipped with a thermal conductivity detector (TCD) using a porapak Q packed column (2 m). Ar (35 mL min^{-1}) was used as the carrier gas, and the temperatures for columns and TCD were 60 and 80°C , respectively. Gases in the stainless-steel autoclave were collected by using a commercial gas-bag and then carried into GC by Ar. H_2O_2 selectivity and H_2 conversion were calculated on the basis of the following formulas:

$$\text{H}_2\text{O}_2 \text{ selectivity} = \frac{n(\text{H}_2\text{O}_2)_{\text{out}}}{n(\text{H}_2\text{O}_2)_{\text{out}} + n(\text{H}_2\text{O})_{\text{out}}} \times 100\% \quad (1)$$

The H_2 conversion was calculated as follows:

$$\text{H}_2 \text{ conversion} = \frac{n(\text{H}_2)_{\text{in}} - n(\text{H}_2)_{\text{out}}}{n(\text{H}_2)_{\text{in}}} \times 100\% \quad (2)$$

H_2O_2 Decomposition and Hydrogenation. For the evaluation of H_2O_2 decomposition ($\text{H}_2\text{O}_2 \rightarrow \text{O}_2 + \text{H}_2\text{O}$), 5 mg of catalyst, 6.8 mL of CH_3OH , 1.45 mL of H_2O , and 0.25 mL of H_2O_2 (30 wt %) were added into the reactor. Afterward, 3.6 MPa of pure N₂ was pressurized into the reactor. The reaction conditions for H_2O_2 decomposition are exactly the same with those for DHS. For the evaluation of H_2O_2 hydrogenation ($\text{H}_2\text{O}_2 + \text{H}_2 \rightarrow 2\text{H}_2\text{O}$), 5 mg of catalyst, 6.8 mL of CH_3OH , 1.45 mL of H_2O , and 0.25 mL of H_2O_2 (30 wt %) were added into the stainless-steel autoclave. 3.6 MPa of H_2/Ar ($\text{H}_2/\text{Ar} = 5\%/\text{95}\%$) was pressurized into the reactor. The reaction conditions for H_2O_2 hydrogenation are the same with those for H_2O_2 decomposition. H_2O_2 decomposition and hydrogenation rates were calculated as follows:

$$\begin{aligned} & \text{H}_2\text{O}_2 \text{ decomposition rate} \\ &= \frac{n(\text{H}_2\text{O}_2)_{\text{in}} - n(\text{H}_2\text{O}_2)_{\text{out}}}{W_{\text{catalyst}} \times t} \times 100\% \end{aligned} \quad (3)$$

$$\begin{aligned} & \text{H}_2\text{O}_2 \text{ hydrogenation rate} \\ &= \frac{n(\text{H}_2\text{O}_2)_{\text{in}} - n(\text{H}_2\text{O}_2)_{\text{out}}}{W_{\text{catalyst}} \times t} \times 100\% \end{aligned} \quad (4)$$

2.6. Computational Methods. Periodic density functional theory (DFT) calculations were performed using Vienna ab initio simulation package (VASP 5.4.4).²⁶ The electron–ion interactions and the interactions between electrons were described by projector augmented wave (PAW) method and generalized gradient approximation (GGA) with the Perdew–Burke–Ernzerhof (PBE) exchange-correlation functional.²⁷ The plane wave basis was expanded to a cutoff energy of 400 eV and the Monkhorst–Pack k-point meshes of $3 \times 3 \times 1$. The electron self-consistent calculations are considered to be converged when the energy differences are less than 10^{-5} eV. The structure optimizations are considered converged when force differences are less than 0.01 eV \AA^{-1} . The semiempirical dispersion corrected DFT-D3 scheme proposed by Grimme²⁸ is used to describe the van der Waals interactions. The spin polarization effect was taken into consideration. We used the experimental lattice constant of bulk Pd (3.89 Å) to construct the Pd (111) surfaces.²⁹ The simulated model of Pd (111) is a 4×4 supercell which consists of four-atomic-layer slab with a vacuum region of 15 Å in the z direction. The top two layers were relaxed and the bottom two layers were fixed during the optimization. The free energy of structure A (GA) was given by

$$G = EA + ZPE - TS$$

where the total energy (EA), zero-point energy (ZPE), and the entropy (S) of each adsorbed state were yielded from DFT calculation, and the thermodynamic corrections for gas molecules were obtained from standard tables.

3. RESULTS AND DISCUSSION

Typically, Pd_xPb NRs were prepared via a simple wet-chemical method, in which $\text{Na}_2\text{PdCl}_4/\text{PbC}_2\text{O}_4$, $\text{Mo}(\text{CO})_6$, DTAB, and PVP/DMF as solvent were used as the precursors, reducing agent, shape directing agent, and solvent, respectively. The compositions of Pd_xPb NRs were tuned by solely altering the amount of PbC_2O_4 , while the other parameters were kept identical during synthesis (see **Experimental Section** for detailed information). TEM images show that Pd_xPb NRs

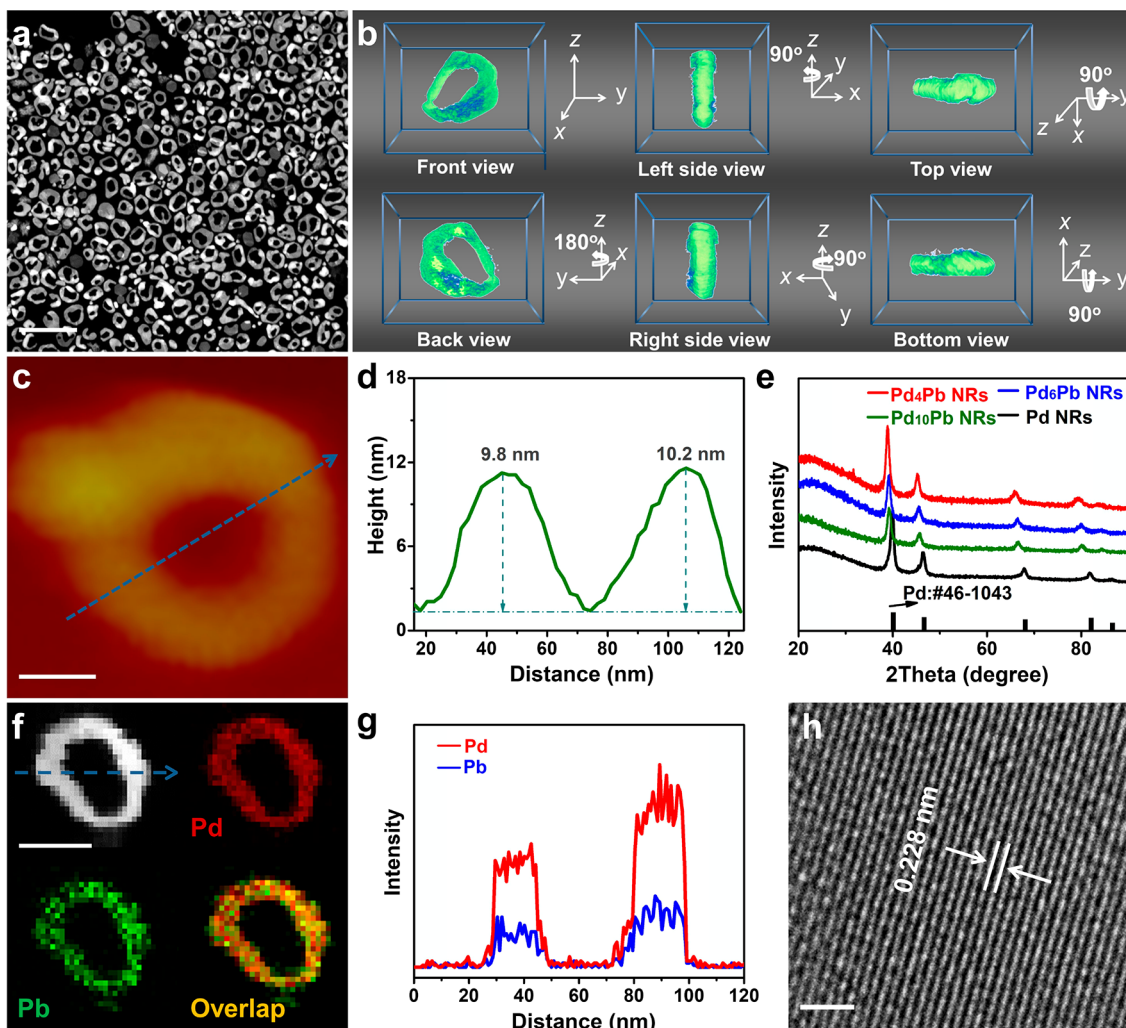


Figure 1. Morphology and composition profile analysis of Pd_6Pb NRs. (a) HAADF-STEM image of Pd_6Pb NRs. (b) Six projected images of a 3D visualization of tomographic reconstruction images of Pd_6Pb NRs. (c) AFM image of Pd_6Pb NRs. (d) Corresponding height profiles of Pd_6Pb NRs. (e) XRD patterns of Pd NRs and Pd_xPb NRs, (f) HAADF-STEM image and elemental mappings, (g) line-scanning analysis, and (h) HRTEM image of Pd_6Pb NRs. The scale bars in (a), (c), (f), and (h) are 200, 20, 50, and 1 nm, respectively.

with different contents of Pd and Pb have been successfully obtained (Figures S1 and S2). Taking Pd_6Pb NRs as an example, HAADF-STEM (Figure 1a) and TEM (Figure S1) images demonstrate that the obtained Pd_6Pb NRs give a shape of nanoring with an average inside diameter of ~ 27 nm and outside diameter of ~ 58 nm (Figure S3). Three-dimensional (3D) tomographic reconstruction based on 2D TEM images at the consecutive tilt angles from -60° to 60° with 4° intervals were performed to further reveal the structure of Pd_6Pb NRs (Figure S4). As depicted in Figure 1b, six projected images of 3D visualization of tomographic reconstruction of Pd_6Pb NRs obviously suggested that Pd_6Pb NRs had a ring-shape structure in spite of slight differences in thickness. More detailed animated voxel recordings of the rotation of tomogram information on Pd_6Pb NRs are shown in Video S1. Moreover, results from atomic force microscopy (AFM) measurement displayed that the average thickness of Pd_6Pb NRs was ~ 10 nm (Figures 1c,d and S5). The characteristic peaks in the XRD pattern were ascribed to the face-centered cubic (fcc) Pd (JCPDS No. 46-1043), and the slight shift of the diffraction peaks to lower angle with the increased Pb content was attributed to the lattice expansion after Pb introduction

(Figure 1e). EDS element mapping and line scanning measurements suggested that Pd and Pb were evenly distributed in Pd_6Pb NRs (Figure 1f,g). The lattice spacing of Pd_6Pb NRs (0.228 nm) was slightly larger than that of Pd (111) facet (0.225 nm) (Figure 1h), being consistent with results from XRD patterns.

Pd_6Pb NRs on homemade TiO_2 (named as Pd_6Pb NRs/ TiO_2) with a loading amount of 3 wt % (based on Pd) was selected as a model catalyst to optimize the reaction conditions for DHS (Figure S6 and Table S1). Prior to the catalytic test, Pd_6Pb NRs/ TiO_2 was experienced a successive treatment in H_2 ($\text{H}_2/\text{Ar} = 5\%/\text{95}\%$) at 200°C for 1 h and in dry air ($\text{O}_2/\text{N}_2 = 20\%/\text{80}\%$) for another 1 h at the same temperature (named as Pd_6Pb NRs/ $\text{TiO}_2\text{-H-A}$) (Figure S7 and S8). Pd_6Pb NRs/ TiO_2 treated in H_2 ($\text{H}_2/\text{Ar} = 5\%/\text{95}\%$) and dry air ($\text{O}_2/\text{N}_2 = 20\%/\text{80}\%$) at 200°C for 1 h were used as references to further study the effects of pretreatment of catalyst on DHS performance, which were named as Pd_6Pb NRs/ $\text{TiO}_2\text{-H}$ and Pd_6Pb NRs/ $\text{TiO}_2\text{-A}$, respectively (Figures S7 and S8). Prior to catalytic evaluation, XPS and IR measurements were performed to check the residual capping agents on catalysts. The absence of Br and Cl peaks in the XPS spectra and the

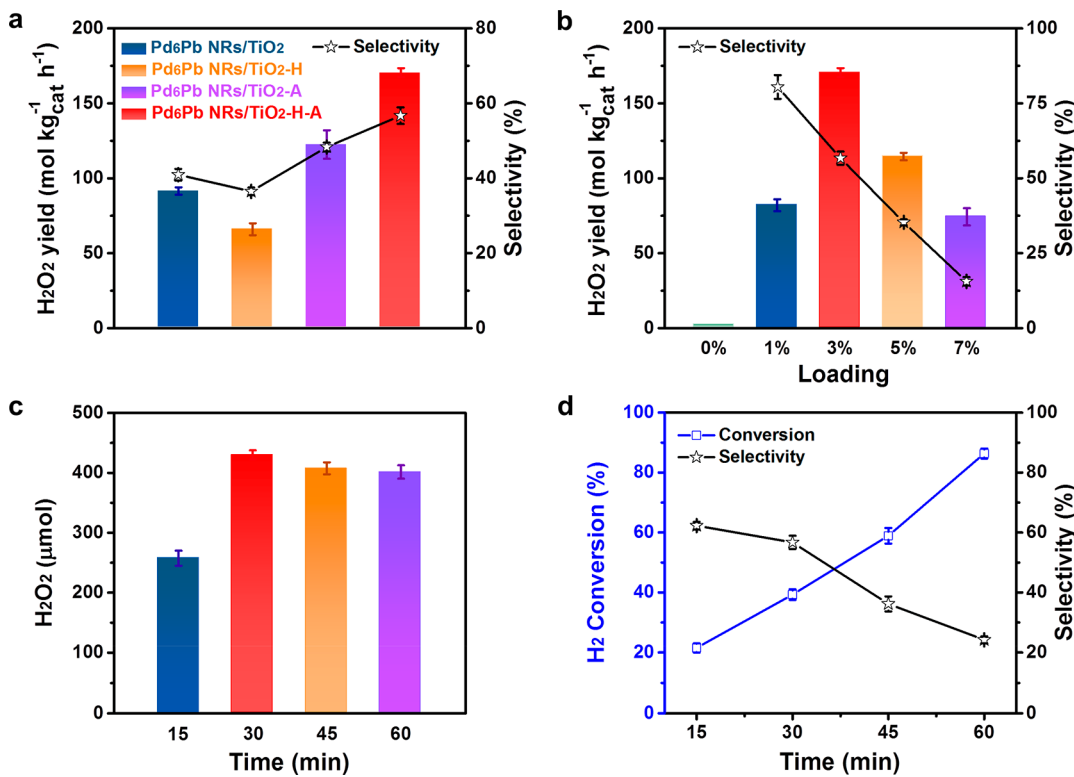


Figure 2. Direct H₂O₂ synthesis on Pd₆Pb NRs/TiO₂ under different reaction conditions. (a) H₂O₂ yield on different pretreated Pd₆Pb NRs/TiO₂ catalysts. Reaction conditions: V_{CH₃OH} = 6.8 mL, V_{H₂O} = 1.7 mL, H₂/O₂/Ar = 0.18/0.4/3.42 MPa, T = 0 °C, catalyst loading amount: 3 wt %, catalyst weight: 5 mg, stirring: 1000 rpm, and reaction time: 30 min. (b) H₂O₂ yield on Pd₆Pb NRs/TiO₂-H-A with different loading amounts of catalyst. Reaction conditions: V_{CH₃OH} = 6.8 mL, V_{H₂O} = 1.7 mL, H₂/O₂/Ar = 0.18/0.4/3.42 MPa, T = 0 °C, catalyst weight: 5 mg, stirring: 1000 rpm, and reaction time: 30 min. (c) The produced H₂O₂ amount and (d) H₂ conversion and H₂O₂ selectivity on Pd₆Pb NRs/TiO₂-H-A with the increased reaction time. Reaction conditions: V_{CH₃OH} = 6.8 mL, V_{H₂O} = 1.7 mL, H₂/O₂/Ar = 0.18/0.4/3.42 MPa, T = 0 °C, catalyst loading amount: 3 wt %, catalyst weight: 5 mg, and stirring: 1000 rpm.

characteristic bands of surfactants in the IR spectra indicates that most of the capping agents have been removed during the washing process (Figure S9).^{30–34} XPS measurement was performed to further investigate the changes in the surface properties of the catalysts under different treatment. As shown in Figure S10, two peaks appeared at the binding energy of 334.6 and 339.9 eV, which were ascribed as Pd 3d 5/2 and Pd 3d 3/2, respectively. By contrast, Pb was a mixture of Pb²⁺ and Pb⁰ in Pd₆Pb NRs/TiO₂, Pd₆Pb NRs/TiO₂-H, Pd₆Pb NRs/TiO₂-A, and Pd₆Pb NRs/TiO₂-H-A (Figure S10b). Further analysis indicated that the ratios of Pb²⁺ and Pb⁰ (Pb²⁺/Pb⁰) were different among those catalysts (Figure S10c), indicating that the variation in the surface properties of catalysts under different treatments. Moreover, HRTEM measurement was performed on Pd₆Pb NRs/TiO₂-H-A to reveal the structural evolution during the pretreatment. As shown in Figure S11, it was found that the ring shape was maintained in Pd₆Pb NRs/TiO₂-H-A, and the lattice spacing of 0.23 nm (Figure S11b) was close to that of Pd₆Pb NRs (0.228 nm, Figure 1h). Results from the SEM-EDS spectrum displayed that the ratio of Pd to Pb on Pd₆Pb NRs/TiO₂-H-A was 84.7:15.3, being consistent with that of Pd₆Pb NRs (84.5:15.5) (Figure S11c). EDS element mapping indicated that Pd and Pb were evenly distributed in Pd₆Pb NRs/TiO₂-H-A (Figure S11d). Figure 2a shows the DHS performance over different catalysts. To further study the effects of pretreatment of catalyst on DHS performance, Pd₆Pb NRs/TiO₂ treated in H₂ (H₂/Ar = 5% / 95%) and dry air (O₂/N₂ = 20%/80%) at 200 °C for 1 h were

used as references, which were named as Pd₆Pb NRs/TiO₂-H and Pd₆Pb NRs/TiO₂-A, respectively. Compared with other catalysts (e.g., Pd₆Pb NRs/TiO₂ without pretreatment, Pd₆Pb NRs/TiO₂-H, Pd₆Pb NRs/TiO₂-A), Pd₆Pb NRs/TiO₂-H-A gives the highest H₂O₂ selectivity of 56.7% and the highest H₂O₂ yield of 170.1 mol kg_{cat}⁻¹ h⁻¹ under the same conditions (Figure 2a). Moreover, the effects of loading amount and reaction time on the DHS performance were studied on Pd₆Pb NRs/TiO₂-H-A. As shown in Figures 2b and S12, when pure TiO₂ was used as catalyst, no H₂ conversion was detected, indicating that TiO₂ was inactive for DHS. H₂ conversion gradually increased from 13.3% to 62.4% when the loading amount of catalyst was increased from 1% to 7%. On the contrary, the selectivity of H₂O₂ obviously decreased with the increased loading amount of catalyst. Typically, H₂O₂ selectivity was 80.5% when the loading amount was 1%, which dropped to 15.6% when the loading amount was 7%. As a result, a volcano shape of H₂O₂ yield was obtained as increasing the loading amount of catalyst. For instance, no H₂O₂ yield was detected on pure TiO₂, while H₂O₂ yield significantly increased to 170.1 mol kg_{cat}⁻¹ h⁻¹ when the loading amount was 3 wt %. A further increase in the loading amount of catalyst would lead to a decrease of H₂O₂ yield, suggesting that H₂O₂ synthesis and side reactions competitively occurred during DHS (Figure 2b). Furthermore, the effects of reaction time on DHS were studied. It was shown that the amount of produced H₂O₂ experienced a significant increase in the first 30 min and a slight decay in the next 30

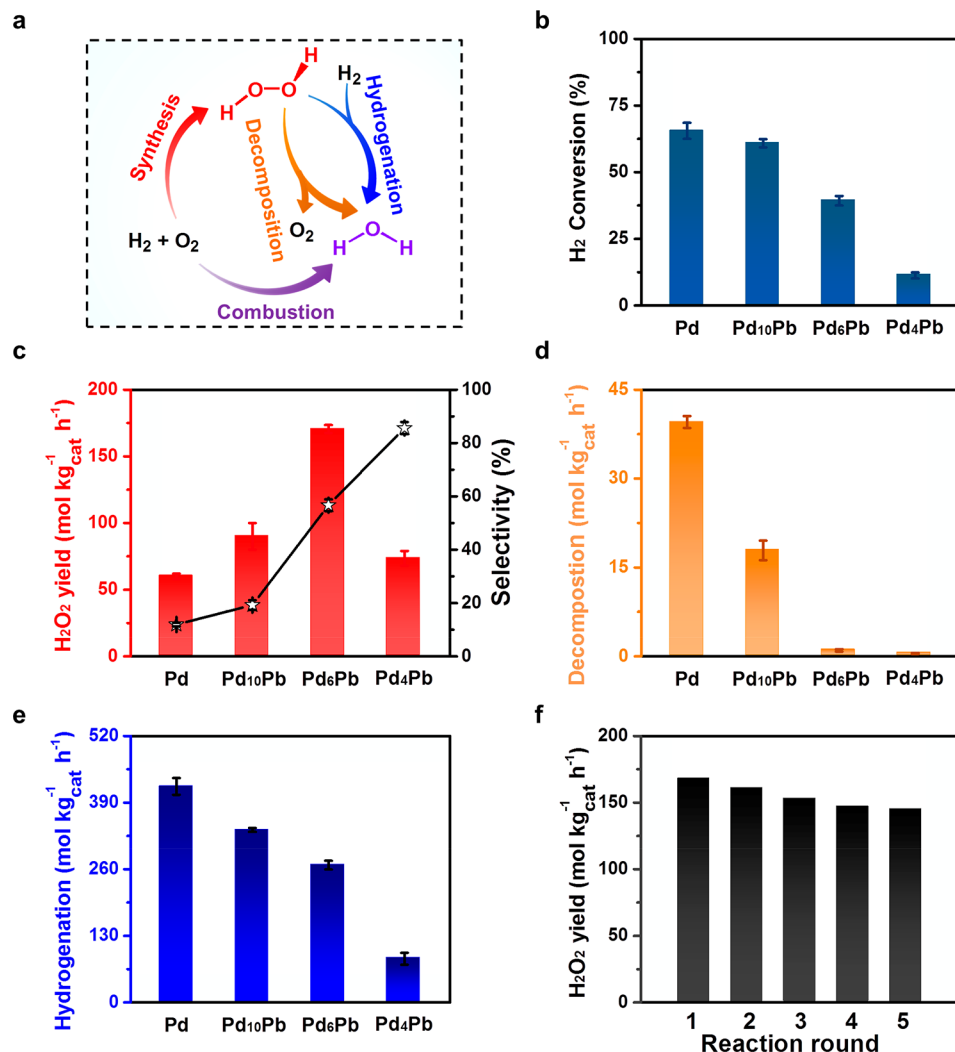


Figure 3. Direct H_2O_2 synthesis on Pd NRs/TiO₂-H-A and Pd_xPb NRs/TiO₂-H-A. (a) Scheme of the direct H_2O_2 synthesis. (b) H_2 conversion, (c) H_2O_2 selectivity and yield on Pd NRs/TiO₂-H-A and Pd_xPb NRs/TiO₂-H-A. (d) H_2O_2 decomposition and (e) H_2O_2 hydrogenation on Pd NRs/TiO₂-H-A and Pd_xPb NRs/TiO₂-H-A. (f) Stability test on Pd₆Pb NRs/TiO₂-H-A in 5 cycles. Reaction conditions for (b), (c), and (f): $V_{\text{CH}_3\text{OH}} = 6.8 \text{ mL}$, $V_{\text{H}_2\text{O}} = 1.7 \text{ mL}$, $\text{H}_2/\text{O}_2/\text{Ar} = 0.18/0.4/3.42 \text{ MPa}$, $T = 0^\circ\text{C}$, loading amount: 3 wt %, catalyst weight: 5 mg, stirring: 1000 rpm, and reaction time: 30 min. Reaction conditions for (d): $V_{\text{CH}_3\text{OH}} = 6.8 \text{ mL}$, $V_{\text{H}_2\text{O}} = 1.45 \text{ mL}$, $V_{\text{H}_2\text{O}_2} = 0.25 \text{ mL}$, $N_2 = 4.0 \text{ MPa}$, $T = 0^\circ\text{C}$, loading amount: 3 wt %, catalyst weight: 5 mg, stirring: 1000 rpm, and reaction time: 30 min. Reaction conditions for (e): $V_{\text{CH}_3\text{OH}} = 6.8 \text{ mL}$, $V_{\text{H}_2\text{O}} = 1.45 \text{ mL}$, $V_{\text{H}_2\text{O}_2} = 0.25 \text{ mL}$, $\text{H}_2/\text{Ar} = 0.18/3.42 \text{ MPa}$, $T = 0^\circ\text{C}$, loading amount: 3 wt %, catalyst weight: 5 mg, stirring: 1000 rpm, and reaction time: 30 min.

min (Figure 2c). To figure out the above-mentioned phenomenon, we further calculated H_2 conversion and H_2O_2 selectivity. As shown in Figure 2d, H_2 conversion gradually increased from 21.5% to 86.3%, while H_2O_2 selectivity obviously decreased from 62.5% to 24.2% with the prolonged reaction time from 15 to 60 min. The obvious decay in H_2O_2 selectivity implied that H_2O_2 decomposition and hydrogenation tended to occur after the accumulation of the continuously produced H_2O_2 in the batch reaction system.⁸ On the basis of the above results, the conditions for pretreatment of catalysts and direct H_2O_2 synthesis were fixed. In particular, the catalysts were subjected to a successive treatment in H_2 ($\text{H}_2/\text{Ar} = 5\%/95\%$) at 200 °C for 1 h and in dry air ($\text{O}_2/\text{N}_2 = 20\%/80\%$) at 200 °C for another 1 h. The loading amount and reaction time were 3 wt % and 30 min, respectively, unless specifically noted.

Pd NRs/TiO₂-H-A, Pd₁₀Pb NRs/TiO₂-H-A, Pd₆Pb NRs/TiO₂-H-A, and Pd₄Pb NRs/TiO₂-H-A were used as catalysts to systematically study the various reaction paths involved in DSH under the above-optimized reaction conditions (Figure 3a). It was found that Pb addition in Pd_xPb NRs led to a decay in H_2 conversion (Figure 3b). For instance, H_2 conversion is 65.5% when Pd NRs/TiO₂-H-A was used as catalyst, which decreased to 11.3% when Pd₄Pb NRs/TiO₂-H-A was used as catalyst. By contrast, the increase of Pb amount in Pd_xPb NRs exhibited a positive influence on H_2O_2 selectivity, as depicted in Figure 3c. H_2O_2 selectivity dramatically jumped to 85.6% when Pd₄Pb NRs/TiO₂-H-A was used as catalyst, which was significantly higher than that of Pd NRs/TiO₂-H-A (11.9%). Consequently, a volcano shape of H_2O_2 yield was observed with the increased Pb amount in Pd_xPb NRs. Specifically, Pd₆Pb NRs/TiO₂-H-A gave the highest H_2O_2 yield of 170.1 $\text{mol kg}_{\text{cat}}^{-1} \text{h}^{-1}$, which was ~2.8 times that of Pd NRs/TiO₂-H-A.

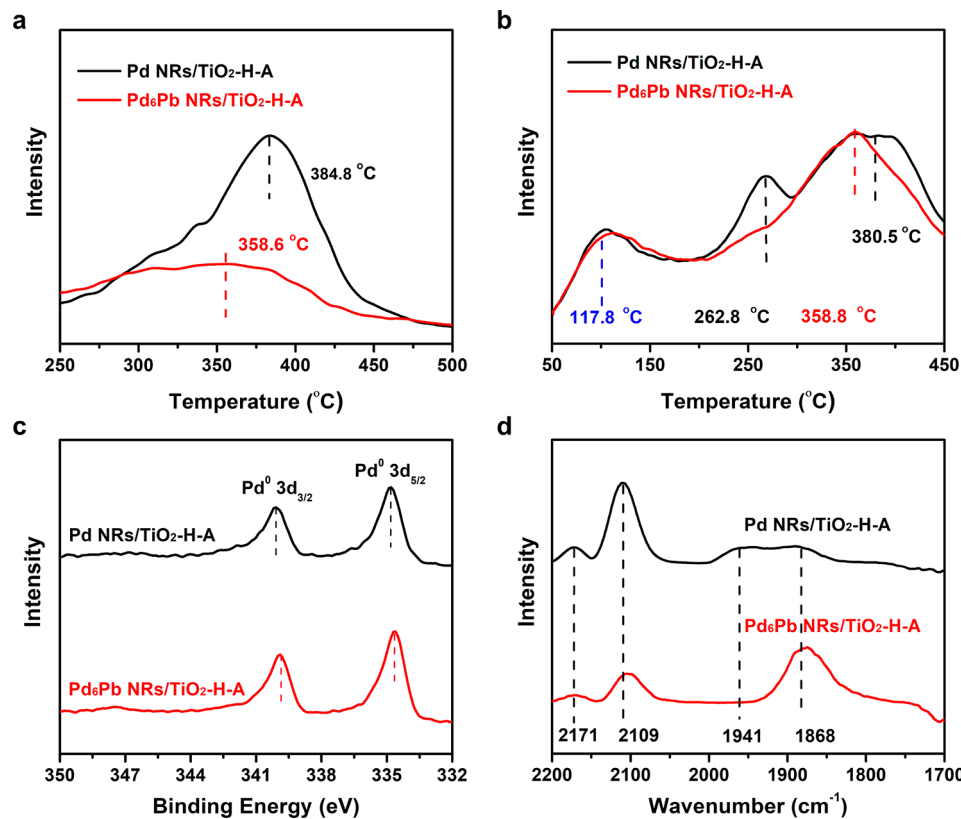


Figure 4. Surface properties analysis of catalysts. (a) H₂-TPD curves, (b) O₂-TPD curves, (c) Pd 3d XPS spectra, and (d) CO-DRIFTS spectra of Pd NRs/TiO₂-H-A and Pd_xPb NRs/TiO₂-H-A.

A (60 mol kg_{cat}⁻¹ h⁻¹) (Figure 3c). To the best of our knowledge, the current H₂O₂ yield on Pd_xPb NRs/TiO₂-H-A has outperformed most of the reported catalysts in the literature (Table S2). Furthermore, H₂O₂ decomposition and hydrogenation in the reaction system were evaluated. As shown in Figure 3d, H₂O₂ decomposition rates for Pd NRs/TiO₂-H-A and Pd_xPb NRs/TiO₂-H-A were 39.5 and 0.6 mol kg_{cat}⁻¹ h⁻¹, respectively, indicating that H₂O₂ decomposition was strikingly suppressed after Pb introduction. Moreover, H₂O₂ hydrogenation on Pd_xPb NRs/TiO₂-H-A was investigated. As shown in Figure 3e, a similar trend was observed on H₂O₂ hydrogenation rate with the increased Pb in Pd_xPb NRs. In particular, H₂O₂ rapidly reacted with H₂ to form H₂O under the reaction conditions, giving a hydrogenation rate of 421.5 mol kg_{cat}⁻¹ h⁻¹ on Pd NRs/TiO₂-H-A. H₂O₂ hydrogenation was strongly suppressed when Pd_xPb NRs/TiO₂-H-A was used as catalyst. For instance, H₂O₂ hydrogenation rate sharply decreased to 85.2 mol kg_{cat}⁻¹ h⁻¹ on Pd_xPb NRs/TiO₂-H-A (Figure 3e). These above results vividly suggested that the synergies in Pd_xPb NRs could not only greatly promote the H₂O₂ synthesis but also obviously suppressed the side reactions, leading to a significant enhancement on DHS performance. In addition, the durability of the catalyst was studied by testing Pd_xPb NRs/TiO₂-H-A in 5 consecutive rounds. It was shown that ring-shaped structure and composition of Pd_xPb NRs were preserved after 5 rounds, suggesting the good stability of Pd_xPb NRs under the indicated conditions (Figure S13). No obvious decay in H₂O₂ yield indicated that Pd_xPb NRs/TiO₂-H-A could serve as an efficient catalyst for DHS (Figure 3f). Note that the slight decay in H₂O₂ yield was likely attributed to the catalyst loss during the recycling. ICP-MS measurement was further performed to

evaluate the stability of Pd_xPb NRs/TiO₂-H-A for DHS. The content of Pb in the solution after 2 h of DHS was as low as 0.016 ppb, suggesting Pd_xPb NRs was stable under the indicated conditions (Figure S14).

To reveal the mechanism of DHS on Pd_xPb NRs/TiO₂-H-A, temperature-programmed desorption (TPD) measurement was performed using H₂ and O₂ as the probe molecules. Here, Pd NRs/TiO₂-H-A was used as a reference. As shown in Figure 4a, a broad and intense peak appeared at ~384.8 °C in the H₂-TPD curve of Pd NRs/TiO₂-H-A, while a weak peak was observed at ~358.6 °C in the H₂-TPD curve of Pd_xPb NRs/TiO₂-H-A. The decrease in peak intensity and peak shift to low temperature implied that Pd_xPb NRs/TiO₂-H-A exhibited a much weaker H₂ adsorption in comparison to Pd NRs/TiO₂-H-A. For O₂-TPD, three peaks were observed in the O₂-TPD curve of Pd NRs/TiO₂-H-A at 117.8, 262.8, and 380.5 °C, which were assigned to the desorption peaks of superoxide (O₂⁻), O⁻ species, and the lattice oxygen (O²⁻), respectively (Figure 4b).^{35–38} By contrast, the characteristic peak of O⁻ species at 262.8 °C disappeared in the O₂-TPD curve of Pd_xPb NRs/TiO₂-H-A (Figure 4b), indicating that O₂ activation, especially the cleavage of the O–O bond on O₂, was strongly suppressed on Pd_xPb NRs/TiO₂-H-A. The significant variations in TPD curves suggested the surface properties of catalyst (Pd NRs/TiO₂-H-A) strongly varied after compositing with Pb (Pd_xPb NRs/TiO₂-H-A), as a result of structure-dependent DHS performance, being well consistent with the experimental observations. Compared with Pd NRs/TiO₂-H-A, a much weaker H₂ adsorption on Pd_xPb NRs/TiO₂-H-A resulted in a lower H₂ conversion, whereas the suppression of O–O bond cleavage on Pd_xPb NRs/TiO₂-H-A led to a higher H₂O₂ selectivity.

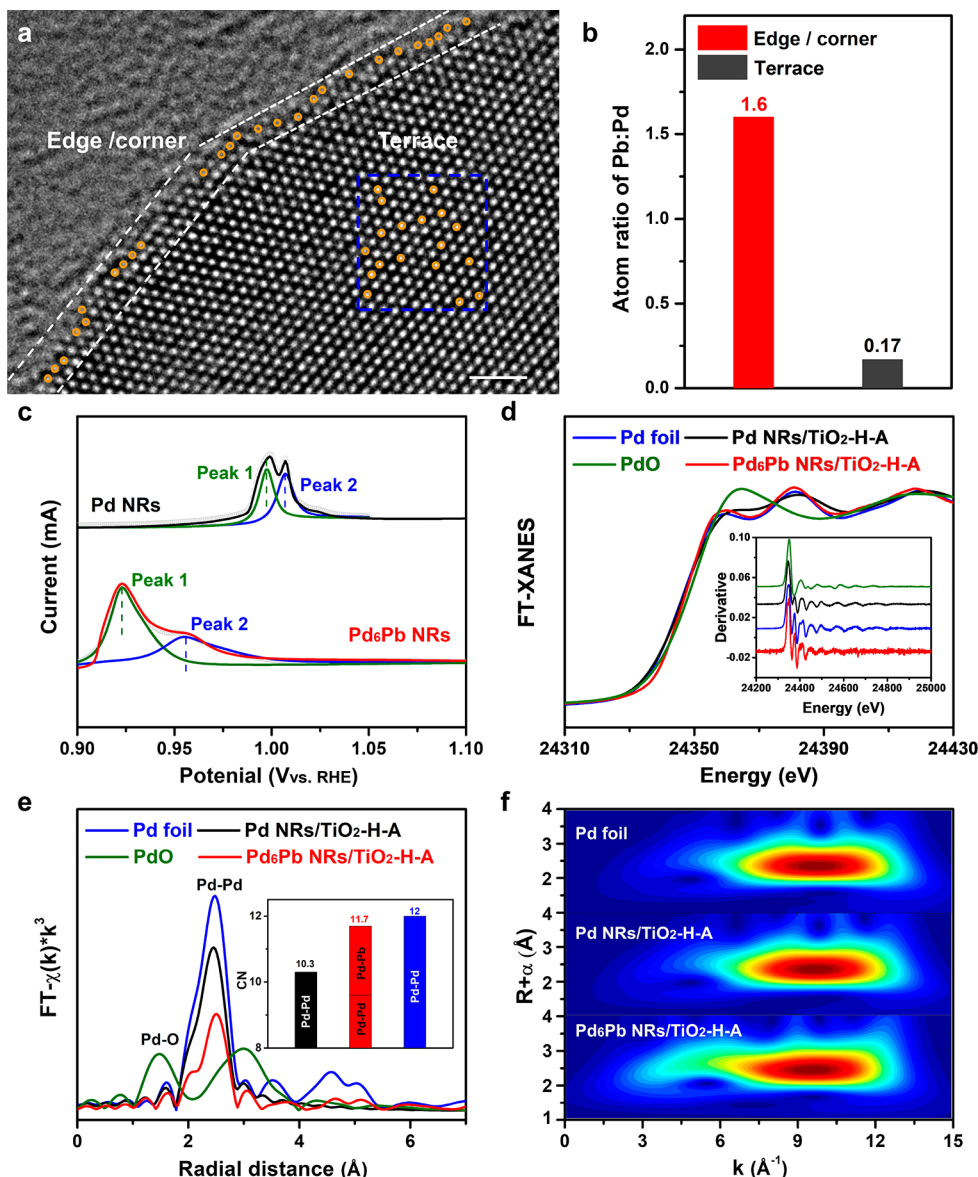


Figure 5. Structural analysis of catalysts. (a) AC-TEM images of Pd₆Pb NRs at the edge, corner, and terrace. The white dotted frame represents edge/corner, and the blue frame represents terrace of NRs. Pb atoms were labeled with dark yellow circles. The scale bar is 1 nm. (b) Atomic ratio of Pb to Pd at edge/corner and terrace determined from AC-TEM image in (a). (c) CO stripping voltammograms of Pd NRs and Pd₆Pb NRs in 0.1 M HClO₄ solution with a scan rate of 20 mV s⁻¹ at 25 °C. (d) XANES spectra of Pd NRs/TiO₂-H-A, Pd₆Pb NRs/TiO₂-H-A and references. Inset shows the first-order derivative of XANES spectrum at Pd K-edge. (e,f) Fourier-transformed EXAFS spectra of Pd NRs/TiO₂-H-A, Pd₆Pb NRs/TiO₂-H-A, and references.

X-ray photoelectron spectroscopy measurement was performed to study the surface properties of catalysts. As shown in Figure 4c, Pd 3d XPS spectrum of Pd NRs/TiO₂-H-A suggested that Pd was in its metallic state (Pd⁰), in which two intense peaks at 334.8 and 340.1 eV corresponding to Pd⁰ 3d_{5/2} and Pd⁰ 3d_{3/2} were observed.³⁹ Compared with Pd NRs/TiO₂-H-A, the characteristic peaks of Pd⁰ in the XPS spectra of Pd_xPb NRs/TiO₂-H-A shifted to lower binding energy (BE) with the increased Pb contents (Figure S15 and Table S3). For instance, the Pd⁰ 3d_{5/2} peak was located at 334.8 eV in the Pd 3d XPS spectrum of Pd NRs/TiO₂-H-A, which slightly shifted to 334.6 eV in Pd 3d XPS spectrum of Pd₆Pb NRs/TiO₂-H-A (Table S3). By contrast, Pb 4f XPS spectra indicated that Pb in Pd_xPb NRs/TiO₂-H-A was a mixture of oxidation state (Pb²⁺) and metallic state (Pb⁰) (Figure S16 and Table S4). Detailed analysis demonstrated that the characteristic peaks of Pb²⁺ and

Pb gradually shifted to higher BE with the increased Pb in Pd_xPb NRs. For instance, the Pb⁰ 4f_{7/2} peak located at 135.9 eV in Pd₁₀Pb NRs/TiO₂-H-A, which obviously shifted to 136.1 eV in Pd₄Pb NRs/TiO₂-H-A. The aforementioned BE shifts in Pd 3d and Pb 4f XPS spectra implied that electrons may transfer from Pb species to Pd in Pd_xPb NRs. Moreover, the surface ratio of Pd to Pb in Pd_xPb NRs/TiO₂-H-A was evaluated by fitting XPS spectra. As shown in Figure S17, the value of Pd/Pb obtained from XPS measurement was obviously lower than those from ICP-AES and EDS measurements, indicating that more Pb atoms were located at the surface of Pd_xPb NRs. Results from XPS measurements further verified the significant changes of surface properties after Pb introduction. Moreover, diffuse reflectance infrared Fourier transform spectroscopy (DRIFTS) measurement was performed on Pd NRs/TiO₂-H-A and Pd₆Pb NRs/TiO₂-H-A

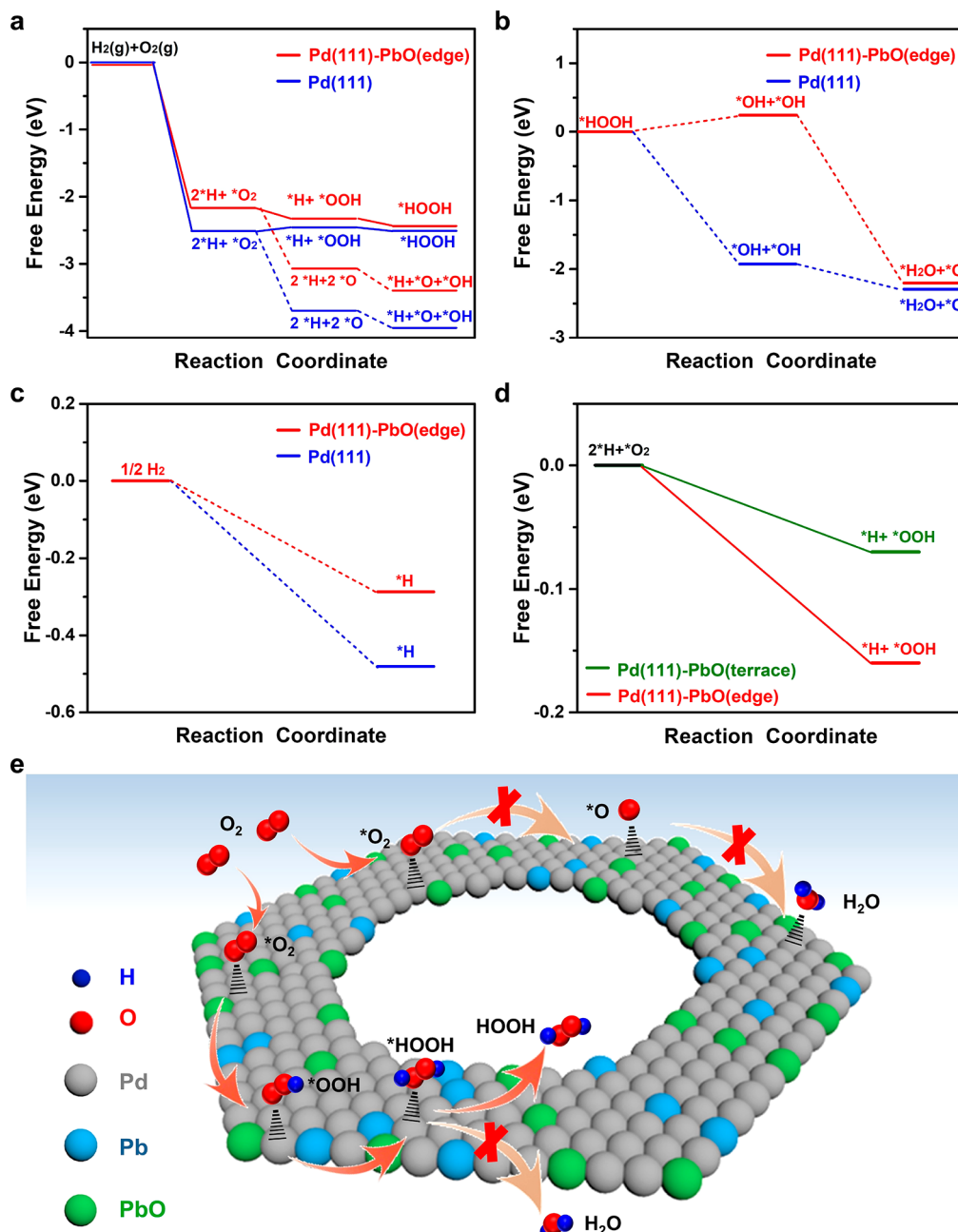


Figure 6. DFT calculations and scheme of H_2O_2 synthesis on Pd_xPb NRs. (a) Energy profiles for H_2O_2 synthesis on $\text{Pd}(111)$ surface and $\text{Pd}(111)\text{-PbO}(\text{edge})$. (b) Energy profiles for H_2O_2 decomposition ($\text{H}_2\text{O}_2 \rightarrow \text{O}_2 + \text{H}_2\text{O}$) on $\text{Pd}(111)$ surface and $\text{Pd}(111)\text{-PbO}(\text{edge})$. (c) Energy profiles for H_2 dissociation ($\text{H}_2 \rightarrow ^*\text{H}$) on $\text{Pd}(111)$ surface and $\text{Pd}(111)\text{-PbO}(\text{edge})$. (d) Energy profiles for $^*\text{OOH}$ formation on $\text{Pd}(111)\text{-PbO}(\text{edge})$ and $\text{Pd}(111)\text{-PbO}(\text{terrace})$. (e) Schematic illustration of H_2O_2 formation on Pd_xPb NRs.

using CO as the probe molecule. As shown in Figure 4d, two intense bands at ~ 2171 and $\sim 2109 \text{ cm}^{-1}$ were observed in the CO-DRIFTS spectrum of Pd NRs/ $\text{TiO}_2\text{-H-A}$, which corresponded to CO linear adsorption on low-coordinated Pd atoms (i.e., corner atoms and edge atoms).^{40,41} Other bands at ~ 1941 and $\sim 1868 \text{ cm}^{-1}$ were assigned to the characteristic peaks of bridged CO and multibonded CO on $\text{Pd}(111)$ facet.^{19,42} For Pd_6Pb NRs/ $\text{TiO}_2\text{-H-A}$, despite the appearance of characteristic peaks at ~ 2171 , ~ 2109 , and 1868 cm^{-1} , the peaks at 2171 and 2109 cm^{-1} corresponding to linear adsorbed CO on low-coordinated Pd obviously weakened in the CO-DRIFTS spectrum of Pd_6Pb NRs/ $\text{TiO}_2\text{-H-A}$. The significant changes in CO-DRIFTS spectra suggest that the arrangement

of surface Pd atoms is different on Pd NRs/ $\text{TiO}_2\text{-H-A}$ and Pd_6Pb NRs/ $\text{TiO}_2\text{-H-A}$, which were consistent with results from TPD and XPS measurements.

Spherical aberration-corrected AC-TEM measurement was performed to observe the atomic structure of Pd_6Pb NRs. As vividly shown in Figure 5a, more Pb atoms (dark spots labeled by yellow cycles) were observed at the corner and edge of NRs, while more Pd atoms (bright spots) are observed at terrace in the AC-TEM image of Pd_6Pb NRs. The lattice distances obtained from AC-TEM image further confirmed the existence of fcc $\text{Pd}(111)$ plane and step atoms in Pd_6Pb NRs (Figure S18). The specific ratio of Pb to Pd atoms (Pb/Pd) at corner/edge and terrace was calculated by counting their numbers.

The Pb/Pd was 1.6 at corner and edge, which was much higher than that at terrace (0.17) (Figure 5b). Similar phenomena were observed on other positions (Figure S19), suggesting that Pb atoms were preferentially located at the edge and corner of Pd_xPb NRs. Considering that atoms at the edge and corner are generally low-coordinated, we may conclude that the amount of low-coordinated Pd atoms significantly decreases after the addition of Pb into Pd NRs. Since low-coordinated Pd atoms at corner and edge generally show much stronger affinity to hydroxyl and CO than those at terrace.⁴³ Additionally, cyclic voltammograms (CV) test and CO stripping voltammograms were performed on Pd NRs and Pd_xPb NRs to further confirm the decrease of low-coordinated Pd atoms in Pd_xPb NRs. The CV test indicated the reduction peak potential of Pd(OH)₂ on Pd NRs was 0.709 V, which was more negative than that of Pd_xPb NRs (0.73 V), indicating Pd NRs manifested stronger hydroxyl adsorption than Pd_xPb NRs (Figure S20).⁴⁴ On the other hand, two sharp CO stripping peaks (labeled as peak 1 and peak 2) corresponding to CO adsorbed on terrace Pd atoms and low-coordinated Pd atoms were observed in CO stripping voltammograms curves (Figures 5c and S21).⁴⁵ Compared with Pd NRs, CO stripping peaks in Pd_xPb NRs shifted to lower potential, suggesting a much weaker CO adsorption on Pd_xPb NRs. The reduced area ratio of peak 2 to peak 1 in CO stripping voltammograms curve of Pd_xPb NRs implied that the amount of low-coordinated Pd in Pd_xPb NRs was lower than that in Pd NRs (Figure 5c), which further confirmed the observation in AC-TEM images.

In addition, XAS measurement was employed to study the structure and the coordination environments of Pd and Pb atoms. Here, Pd foil and PdO were used as references. X-ray adsorption near edge structure (XANES) spectra at Pd K-edge are shown in Figure 5d. Both Pd NRs/TiO₂-H-A and Pd_xPb NRs/TiO₂-H-A exhibited similar features with Pd foil in the XANES spectra (Figure 5d), and no obvious energy shift of Pd K-edge was observed in the first-order derivative of XANES spectrum (inset of Figure 5d), which further confirmed the metallic state of Pd in these samples. However, only the feature of Pd–Pd coordination was observed in the EXAFS spectra of Pd NRs/TiO₂-H-A and Pd_xPb NRs/TiO₂-H-A (Figure 5e,f), which was in agreement with results from XANES and XPS measurements. Detailed fitting of EXAFS spectra demonstrates that the Pd–Pd coordination number (CN) in Pd NRs/TiO₂-H-A (10.3 ± 1.0) was lower than that in Pd foil (12) (Figure S22 and Table S5), which was attributed to the existence of low-coordinated Pd atoms in Pd NRs that greatly reduced the overall Pd–Pd CN in Pd NRs. After compositing with Pb (i.e., Pd_xPb NRs/TiO₂-H-A), significant variations were observed in the Pd coordination environment. The appearance of Pd–Pb coordination (2.1 ± 0.2) suggested that partial Pd atoms were replaced by Pb atoms in Pd_xPb NRs, leading to a decrease in the CN of Pd–Pd (9.6 ± 0.7).

The reaction mechanism of DHS was investigated in atomic details by carrying out DFT calculations. The simulation model of Pd_xPb NRs was built from four layers of fcc Pd (111) surface, in which six Pd atoms were removed at the first layer to simulate the Pd coordination environment on the basis of the observations in AC-TEM images. Furthermore, one Pd atom at the edge was replaced by one Pb atom associated with an O atom. The final simulation model named as Pd(111)–PbO(edge) is shown in Figure S23. The reaction pathway of H₂O₂ formation follows this process of *O₂ → *OOH → *HOOH. As one of the main side reactions, *O₂ may be

further converted into *O to the formation of H₂O in the presence of H₂ (*O₂ → *O → *H₂O). Therefore, DFT calculations were carried out to investigate the formation energies of these above species (e.g., *O₂, *O, *OOH, and *HOOH) on Pd(111)–PbO(edge) and Pd(111) surface. Results are shown in Figure 6. On the Pd(111) surface, the energy for *OOH formation is 0.052 eV, while the energy for *O formation is -1.18 eV, implying that Pd(111) surface tends to dissociate *O₂ to *O and further form H₂O in the presence of H₂ (Figures 6a and S23). The formation energy of *OOH on Pd(111)–PbO(edge) is -0.16 eV, which is much lower than that on the Pd(111) surface. On the other hand, the formation energy for *O on Pd(111)–PbO(edge) is obviously higher than that on the Pd(111) surface (-0.90 eV vs -1.18 eV), indicating that O₂ dissociation is strongly suppressed on Pd(111)–PbO(edge) in comparison to the Pd(111) surface (Figure 6a). Additionally, the reaction barrier for the step of *OOH formation was also investigated. As shown in Figure S24, the energy barrier for 2*H + *O₂ → *H + *OOH was only 0.31 eV on Pd(111)-PbO(edge), which was much lower than that on pure Pd(111) reported by Quon et al. (1.12 eV)⁴⁶ and Tian et al. (0.58 eV),⁴⁷ indicating the *OOH formation was thermodynamically and kinetically favorable on the Pd(111)-PbO(edge) compared with Pd(111). Consequently, DFT calculations show that Pd(111)–PbO(edge) is much more thermodynamically and kinetically favorable than Pd(111) surface for H₂O₂ formation, while Pd(111) surface tends to dissociate O₂ to produce H₂O in the presence of H₂, which is well consistent with the experimental observations.

H₂O₂ decomposition and hydrogenation is regarded as another two main side reactions to reduce yield of H₂O₂. Here, the decomposition and hydrogenation of H₂O₂ on Pd(111)–PbO(edge) and Pd(111) surface were further simulated by DFT calculations, as depicted in Figure 6b,c. It was found that the Pd(111) surface tended to decompose H₂O₂ to form H₂O and O₂ via an intermediate of *OH by breaking the O–O in H₂O₂ (Figure 6b). By contrast, the formation energy of *OH was 0.25 eV on Pd(111)–PbO(edge), which was much higher than that on Pd(111) surface (-1.93 eV), indicating that the cleavage of O–O in H₂O₂ on Pd(111)–PbO(edge) was dramatically suppressed (Figure 6b). Since H₂O₂ decomposition (H₂O₂ → 2*OH) and H₂ activation (H₂ → 2*H) were involved in H₂O₂ hydrogenation, we further calculated the formation energy of *H on Pd(111)–PbO(edge) and Pd(111) surface. As shown in Figure 6c, the formation energies of *H were -0.28 eV and -0.48 eV on Pd(111)–PbO(edge) and Pd(111) surface, respectively, suggesting that the Pd(111) surface was more favorable for H₂ activation than Pd(111)–PbO(edge). In other words, H₂O₂ hydrogenation was allowed on Pd NRs, but strongly suppressed on Pd_xPb NRs. In addition, we calculated the formation energy of *OOH when PbO preferentially locates at the terrace (labeled as Pd(111)–PbO(terrace)) (Figure 6d and Figure S25). The formation energy of *OOH on Pd(111)–PbO(terrace) was -0.07 eV, which was higher than that on Pd(111)–PbO(edge) (-0.16 eV) but obviously lower than that on Pd(111) surface (0.052 eV), suggesting that the present Pd_xPb NRs (Pd(111)–PbO(edge)) could serve as highly efficient catalyst for DHS. On the basis of the DFT calculations, we may conclude that Pd_xPb NRs can promote the formation of *OOH, a key intermediate for H₂O₂, but strongly suppress the cleavage of O–O in O₂ and H₂O₂, leading to an enhanced DHS performance (Figure 6e).

4. CONCLUSIONS

To conclude, we here demonstrate an efficient DHS catalyst of Pd_xPb NRs via surface modification. Characterizations indicate that Pb species preferentially locate at the edge and corner of NRs, leading to a significant decrease of low-coordinated Pd atoms in Pd_xPb NRs. As a result, Pd_xPb NRs greatly promote the formation of *OOH, a critical intermediate for H₂O₂ formation, but strongly inhibit the O₂ dissociation and H₂O₂ degradation. The optimized Pd_xPb NRs/TiO₂-H-A gives a H₂O₂ yield of 170.1 mol kg_{cat}⁻¹ h⁻¹, being one of the best catalysts for direct H₂O₂ synthesis reported to the best of our knowledge. The significance of surface modification on direct H₂O₂ synthesis highlighted in the current work, which has been further backed by detailed characterizations, experimental observations, and theoretical calculations, may guide chemists to design catalysts a reasonable and cost-effective way.

■ ASSOCIATED CONTENT

Supporting Information

The Supporting Information is available free of charge at <https://pubs.acs.org/doi/10.1021/acscatal.0c04348>.

Experimental details and data; Figures S1–25 and Tables S1–S5 ([PDF](#))

Video S1 ([MPG](#))

■ AUTHOR INFORMATION

Corresponding Authors

Yong Xu — Institute of Functional Nano & Soft Materials (FUNSOM), Jiangsu Key Laboratory for Carbon-Based Functional Materials and Devices, Soochow University, Jiangsu 215123, China; Guangzhou Key Laboratory of Low-Dimensional Materials and Energy Storage Devices, Collaborative Innovation Center of Advanced Energy Materials, School of Materials and Energy, Guangdong University of Technology, Guangzhou 510006, Guangdong, China; [orcid.org/0000-0001-5115-6492](#); Email: yongxu@gdut.edu.cn

Xiaoqing Huang — College of Chemistry, Chemical Engineering and Materials Science, Soochow University, Jiangsu 215123, China; College of Chemistry and Chemical Engineering, Xiamen University, Xiamen 361005, China; [orcid.org/0000-0003-3219-4316](#); Email: hxq006@suda.edu.cn, hxq006@xmu.edu.cn

Authors

Kailei Cao — College of Chemistry, Chemical Engineering and Materials Science, Soochow University, Jiangsu 215123, China

Hao Yang — Institute of Functional Nano & Soft Materials (FUNSOM), Jiangsu Key Laboratory for Carbon-Based Functional Materials and Devices, Soochow University, Jiangsu 215123, China; [orcid.org/0000-0002-8241-6231](#)

Shuxing Bai — College of Chemistry, Chemical Engineering and Materials Science, Soochow University, Jiangsu 215123, China

Chengyong Yang — College of Chemistry, Chemical Engineering and Materials Science, Soochow University, Jiangsu 215123, China

Yu Wu — Institute of Functional Nano & Soft Materials (FUNSOM), Jiangsu Key Laboratory for Carbon-Based

Functional Materials and Devices, Soochow University, Jiangsu 215123, China

Miao Xie — Institute of Functional Nano & Soft Materials (FUNSOM), Jiangsu Key Laboratory for Carbon-Based Functional Materials and Devices, Soochow University, Jiangsu 215123, China; [orcid.org/0000-0002-9797-1449](#)

Tao Cheng — Institute of Functional Nano & Soft Materials (FUNSOM), Jiangsu Key Laboratory for Carbon-Based Functional Materials and Devices, Soochow University, Jiangsu 215123, China; [orcid.org/0000-0003-4830-177X](#)

Qi Shao — College of Chemistry, Chemical Engineering and Materials Science, Soochow University, Jiangsu 215123, China; [orcid.org/0000-0002-9858-0458](#)

Complete contact information is available at: <https://pubs.acs.org/10.1021/acscatal.0c04348>

Author Contributions

[#](K.C., H.Y.) These authors contributed equally.

Notes

The authors declare no competing financial interest.

■ ACKNOWLEDGMENTS

This work was financially supported by the Ministry of Science and Technology (2016YFA0204100, 2017YFA0208200), the National Natural Science Foundation of China (21571135, 51802206), Young Thousand Talented Program, Jiangsu Province Natural Science Fund for Distinguished Young Scholars (BK20170003), the Natural Science Foundation of Jiangsu Province (BK20180846), the Priority Academic Program Development of Jiangsu Higher Education Institutions (PAPD), and the start-up fundings from Xiamen University.

■ REFERENCES

- (1) Lane, B. S.; Burgess, K. Metal-catalyzed epoxidations of alkenes with hydrogen peroxide. *Chem. Rev.* **2003**, *103*, 2457–2474.
- (2) De Faveri, G.; Ilyashenko, G.; Watkinson, M. Recent advances in catalytic asymmetric epoxidation using the environmentally benign oxidant hydrogen peroxide and its derivatives. *Chem. Soc. Rev.* **2011**, *40*, 1722–1760.
- (3) Zhao, S.; Zhao, X.; Zhang, H.; Li, J.; Zhu, Y. Covalent combination of polyoxometalate and graphitic carbon nitride for light-driven hydrogen peroxide production. *Nano Energy* **2017**, *35*, 405–414.
- (4) Hall, A. S.; Kondo, A.; Maeda, K.; Mallouk, T. E. Microporous brookite-phase titania made by replication of a metal-organic framework. *J. Am. Chem. Soc.* **2013**, *135*, 16276–16279.
- (5) Bryliakov, K. P. Catalytic asymmetric oxygenations with the environmentally benign oxidants H₂O₂ and O₂. *Chem. Rev.* **2017**, *117*, 11406–11459.
- (6) Edwards, J. K.; Hutchings, G. J. Palladium and gold-palladium catalysts for the direct synthesis of hydrogen peroxide. *Angew. Chem., Int. Ed.* **2008**, *47*, 9192–9198.
- (7) Lari, G. M.; Puertolas, B.; Shahrokh, M.; Lopez, N.; Perez Ramirez, J. Hybrid palladium nanoparticles for direct hydrogen peroxide synthesis: the key role of the ligand. *Angew. Chem.* **2017**, *129*, 1801–1805.
- (8) Campos-Martin, J. M.; Blanco-Brieva, G.; Fierro, J. L. G. Hydrogen peroxide synthesis: an outlook beyond the anthraquinone process. *Angew. Chem., Int. Ed.* **2006**, *45*, 6962–6984.
- (9) Flaherty, D. W. Direct synthesis of H₂O₂ from H₂ and O₂ on Pd catalysts: current understanding, outstanding questions, and research needs. *ACS Catal.* **2018**, *8*, 1520–1527.

- (10) Freakley, S. J.; He, Q.; Harrhy, J. H.; Lu, L.; Crole, D. A.; Morgan, D. J.; Ntaijua, E. N.; Edwards, J. K.; Carley, A. F.; Borisevich, A. Y.; Kiely, C. J.; Hutchings, G. J. Palladium-tin catalysts for the direct synthesis of H_2O_2 with high selectivity. *Science* **2016**, *351*, 965–968.
- (11) Solsona, B. E.; Edwards, J. K.; Landon, P.; Carley, A. F.; Herzing, A.; Kiely, C. J.; Hutchings, G. J. Direct synthesis of hydrogen peroxide from H_2 and O_2 using Al_2O_3 supported Au-Pd catalysts. *Chem. Mater.* **2006**, *18*, 2689–2695.
- (12) García-Serna, J.; Moreno, T.; Biasi, P.; Cocero, M. J.; Mikkola, J. P.; Salmi, T. O. Engineering in direct synthesis of hydrogen peroxide: Targets, reactors and guidelines for operational conditions. *Green Chem.* **2014**, *16*, 2320–2343.
- (13) Edwards, J. K.; Ntaijua N, E.; Carley, A. F.; Herzing, A. A.; Kiely, C. J.; Hutchings, G. J. Direct synthesis of H_2O_2 from H_2 and O_2 over gold, palladium, and gold-palladium catalysts supported on acid-pretreated TiO_2 . *Angew. Chem., Int. Ed.* **2009**, *48*, 8512–8515.
- (14) Farberow, C. A.; Godinez-Garcia, A.; Peng, G. W.; Perez-Robles, J. F.; Solorza-Feria, O.; Mavrikakis, M. Mechanistic studies of oxygen reduction by hydrogen on $PdAg(110)$. *ACS Catal.* **2013**, *3*, 1622–1632.
- (15) Xu, H.; Cheng, D.; Gao, Y. Design of high-performance Pd-based alloy nanocatalysts for direct synthesis of H_2O_2 . *ACS Catal.* **2017**, *7*, 2164–2170.
- (16) Edwards, J. K.; Freakley, S. J.; Carley, A. F.; Kiely, C. J.; Hutchings, G. J. Strategies for designing supported gold-palladium bimetallic catalysts for the direct synthesis of hydrogen peroxide. *Acc. Chem. Res.* **2014**, *47*, 845–854.
- (17) Edwards, J. K.; Thomas, A.; Carley, A. F.; Herzing, A. A.; Kiely, C. J.; Hutchings, G. J. Au-Pd supported nanocrystals as catalysts for the direct synthesis of hydrogen peroxide from H_2 and O_2 . *Green Chem.* **2008**, *10*, 388–394.
- (18) Feng, Y. G.; Shao, Q.; Huang, B. L.; Zhang, J. B.; Huang, X. Q. Surface engineering at the interface of core/shell nanoparticles promotes hydrogen peroxide generation. *Natl. Sci. Rev.* **2018**, *5*, 895–906.
- (19) Wang, S.; Gao, K.; Li, W.; Zhang, J. Effect of Zn addition on the direct synthesis of hydrogen peroxide over supported palladium catalysts. *Appl. Catal., A* **2017**, *531*, 89–95.
- (20) Gao, F.; Goodman, D. W. Pd-Au bimetallic catalysts: Understanding alloy effects from planar models and (supported) nanoparticles. *Chem. Soc. Rev.* **2012**, *41*, 8009–8020.
- (21) Maity, S.; Eswaramoorthy, M. Ni-Pd bimetallic catalysts for the direct Synthesis of H_2O_2 -unusual enhancement of Pd activity in the presence of Ni. *J. Mater. Chem. A* **2016**, *4*, 3233–3237.
- (22) Ouyang, L.; Tian, P.; Da, G.; Xu, X.; Ao, C.; Chen, T.; Si, R.; Xu, J.; Han, Y. The origin of active sites for direct synthesis of H_2O_2 on Pd/ TiO_2 catalysts: Interfaces of Pd and PdO domains. *J. Catal.* **2015**, *321*, 70–80.
- (23) Wilson, N. M.; Flaherty, D. W. Mechanism for the direct synthesis of H_2O_2 on Pd clusters: Heterolytic reaction pathways at the liquid-solid interface. *J. Am. Chem. Soc.* **2016**, *138*, 574–586.
- (24) Wang, F.; Xia, C.; De-Visser, S. P.; Wang, Y. How does the oxidation state of palladium surfaces affect the reactivity and selectivity of direct synthesis of hydrogen peroxide from hydrogen and oxygen gases? A density functional study. *J. Am. Chem. Soc.* **2019**, *141*, 901–910.
- (25) Han, X.; Kuang, Q.; Jin, M.; Xie, Z.; Zheng, L. Synthesis of titania nanosheets with a high percentage of exposed (001) facets and related photocatalytic properties. *J. Am. Chem. Soc.* **2009**, *131*, 3152–3153.
- (26) Kresse, G.; Furthmüller, J. Efficient iterative schemes for ab initio total-energy calculations using a plane-wave basis set. *Phys. Rev. B: Condens. Matter Mater. Phys.* **1996**, *54*, 11169.
- (27) Perdew, J. P.; Burke, K.; Ernzerhof, M. Generalized gradient approximation made simple. *Phys. Rev. Lett.* **1996**, *77*, 3865.
- (28) Grimme, S.; Antony, J.; Ehrlich, S.; Krieg, H. A consistent and accurate ab initio parametrization of density functional dispersion correction (DFT-D) for the 94 elements H-Pu. *J. Chem. Phys.* **2010**, *132*, 154104.
- (29) Eichler, A.; Mittendorfer, F.; Hafner, J. Precursor-mediated adsorption of oxygen on the (111) surfaces of platinum-group metals. *Phys. Rev. B: Condens. Matter Mater. Phys.* **2000**, *62*, 4744–4755.
- (30) Han, G. H.; Lee, S. H.; Seo, M. G.; Lee, K. Y. Effect of polyvinylpyrrolidone (PVP) on palladium catalysts for direct synthesis of hydrogen peroxide from hydrogen and oxygen. *RSC Adv.* **2020**, *10*, 19952–19960.
- (31) Borodko, Y.; Humphrey, S. M.; Tilley, T. D.; Frei, H.; Somorjai, G. A. Charge-transfer interaction of poly(vinylpyrrolidone) with platinum and rhodium nanoparticles. *J. Phys. Chem. C* **2007**, *111*, 6288–6295.
- (32) Choudhary, V. R.; Samanta, C. Role of chloride or bromide anions and protons for promoting the selective oxidation of H_2 by O_2 to H_2O_2 over supported Pd catalysts in an aqueous medium. *J. Catal.* **2006**, *238*, 28–38.
- (33) Fortunato, G. V.; Pizzutilo, E.; Cardoso, E. S. F.; Lanza, M. R. V.; Katsounaros, I.; Freakley, S. J.; Mayrhofer, K. J.; Maia, G.; Ledendecker, M. The oxygen reduction reaction on palladium with low metal loadings: The effects of chlorides on the stability and activity towards hydrogen peroxide. *J. Catal.* **2020**, *389*, 400–408.
- (34) Abazari, R.; Mahjoub, A. R.; Sanati, S. A facile and efficient preparation of anatase titania nanoparticles in micelle nanoreactors: Morphology, structure, and their high photocatalytic activity under UV light illumination. *RSC Adv.* **2014**, *4*, 56406–56414.
- (35) Chon, H.; Pajares, J. Hall effect studies of oxygen chemisorption of zinc oxide. *J. Catal.* **1969**, *14*, 257–260.
- (36) Van-Hooft, J. H. C. Formation of paramagnetic surface species during the oxidation of nonstoichiometric TiO_2 (A), SnO_2 , and ZnO . *J. Catal.* **1968**, *11*, 277–279.
- (37) Iwamoto, M.; Yoda, Y.; Yamazoe, N.; Seiyama, T. Study of metal oxide catalysts by temperature programmed desorption. *J. Phys. Chem.* **1978**, *82*, 2564–2570.
- (38) Zeng, Y.; Wang, T.; Zhang, S.; Wang, Y.; Zhong, Q. Sol-gel synthesis of $CuO-TiO_2$ catalyst with high dispersion CuO species for selective catalytic oxidation of NO. *Appl. Surf. Sci.* **2017**, *411*, 227–234.
- (39) Peng, H. C.; Xie, S.; Park, J. H.; Xia, X.; Xia, Y. Quantitative analysis of the coverage density of Br^- ions on Pd {100} facets and its role in controlling the shape of Pd nanocrystals. *J. Am. Chem. Soc.* **2013**, *135*, 3780–3783.
- (40) Ouyang, L.; Da, G.; Tian, P.; Chen, T.; Liang, G.; Xu, J.; Han, Y. Insight into active sites of Pd-Au/ TiO_2 catalysts in hydrogen peroxide synthesis directly from H_2 and O_2 . *J. Catal.* **2014**, *311*, 129–136.
- (41) Giorgi, J. B.; Schroeder, T.; Baumer, M.; Freund, H. J. Study of CO adsorption on crystalline-silica-supported palladium particles. *Surf. Sci.* **2002**, *498*, L71–L77.
- (42) Gao, F.; Wang, Y.; Goodman, D. W. CO Oxidation over AuPd (100) from ultrahigh vacuum to near-atmospheric pressures: The critical role of contiguous Pd atoms. *J. Am. Chem. Soc.* **2009**, *131*, 5734–5735.
- (43) Gao, D.; Zhou, H.; Wang, J.; Miao, S.; Yang, F.; Wang, G.; Wang, J.; Bao, X. Size-dependent electrocatalytic reduction of CO_2 over Pd nanoparticles. *J. Am. Chem. Soc.* **2015**, *137*, 4288–4291.
- (44) Mayrhofer, K. J. J.; Blizanac, B. B.; Arenz, M.; Stamenkovic, V. R.; Ross, P. N.; Markovic, N. M. The impact of geometric and surface electronic properties of Pt-catalysts on the particle size effect in electrocatalysis. *J. Phys. Chem. B* **2005**, *109*, 14433–14440.
- (45) Xiao, L.; Zhuang, L.; Liu, Y.; Lu, J. Activating Pd by morphology tailoring for oxygen reduction. *J. Am. Chem. Soc.* **2009**, *131*, 602–608.
- (46) Quon, S.; Jo, D. K.; Han, G. H.; Han, S. S.; Seo, M. G.; Lee, K. Y. Role of Pt atoms on Pd(111) surface in the direct synthesis of hydrogen peroxide: Nano-catalytic experiments and DFT calculations. *J. Catal.* **2018**, *368*, 237–247.
- (47) Tian, P. H.; Ouyang, L.; Xu, X. C.; Xu, J.; Han, Y. F. Density functional theory study of direct synthesis of H_2O_2 from H_2 and O_2

on Pd (111), Pd (100), and Pd (110) surfaces. *Chin. J. Catal.* **2013**, *34*, 1002–1012.